Nano Energy 126 (2024) 109638

Contents lists available at ScienceDirect

Nano Energy

journal homepage: www.elsevier.com/locate/nanoen

# A dual-symmetry triboelectric acoustic sensor with ultrahigh sensitivity and working bandwidth

Huake Yang [a,1], Xiao Xiao [b,1], Farid Manshaii [b], Dahu Ren [a], Xiaochuan Li [a], Junyi Yin [b], Qianying Li [a], Xuemei Zhang [a], Shengyang Xiong [a], Yi Xi [a,*], Jun Chen [b,*]

[a] Department of Applied Physics, State Key Laboratory of Power Transmission Equipment & System Security and New Technology, Chongqing Key Laboratory of Soft Condensed Matter Physics and Smart Materials, Key Laboratory of Optoelectronic Technology & Systems, Chongqing University, Chongqing, 400044, China

[b] Department of Bioengineering, University of California, Los Angeles, Los Angeles, CA 90095, USA

ARTICLE INFO

*Keywords:*
Acoustic sensor
Triboelectric
Dual-symmetry
Ultrahigh sensitivity
Working bandwidth

ABSTRACT

Triboelectricity in materials has emerged as an innovative and increasingly researched approach for acoustic sensing. Despite its promise, the field has faced significant challenges due to limited working bandwidth and sensitivity. As a result, we have developed a dual-symmetry triboelectric acoustic sensor (DS-TAS), featuring an expansive working bandwidth from 20 Hz to 200 kHz, exceptional sensitivity of 6.67 V/Pa, and a detection limit as low as 0.002 Pa. Moreover, the DS-TAS has been successfully integrated into a real-time, multi-directional ultrasonic radar system, achieving an impressively minimal detection error of less than 5 mm. This breakthrough in acoustic sensing performance positions the DS-TAS as a significant milestone for the field, with broad applications ranging from human-machine interaction to voice recognition.

## 1. Introduction

Acoustic sensing devices, capable of detecting ambient sound waves, are pivotal in diverse fields including human-computer interaction, intelligent driving, healthcare, environmental monitoring, and wildlife research [1–15]. Among the array of acoustic sensing technologies, materials triboelectricity has emerged as a promising platform. This technology utilizes triboelectrification and electrostatic induction, offering advantages like simple structure, light weight, flexibility, and scalable fabrication processes [16–37]. Demonstrated applications of materials triboelectricity include frequency-selective acoustic and haptic sensors [38], sound-driven triboelectric nanogenerators for underwater communication [39], self-powered triboelectric auditory sensors for hearing aids [40], micro pyramid-patterned triboelectric microphones [41], and triboelectric devices for acoustic energy transfer and signal communication [42]. However, it is important to note that most existing technologies are limited in their ability to measure sound waves effectively only above 94 dB (>1 Pa) and have few applications in the lower decibel range (40–60 dB). Additionally, these systems typically only respond to frequencies up to several kilohertz. This limitation makes it difficult for them to detect acoustic waves in higher frequency ranges, such as ultrasonic frequencies in air, which attenuate rapidly.

Herein, we have developed a dual-symmetry triboelectric acoustic sensor (DS-TAS) for high-performance acoustic sensing. This sensor exhibits a multifaceted performance spectrum, offering continuous responses across the entire audible frequency range, from 20 Hz to 20 kHz. It is also capable of detecting ultrasonic waves at various distinct frequencies, including 25, 40, 58, and 200 kHz. The DS-TAS also distinguishes itself with its remarkable sensitivity, achieving 6.67 V/Pa, and can effectively record sound in the range of 0.002 Pa and 0.02 Pa (40–60 dB). Additionally, we have utilized the DS-TAS to develop a real-time multidirectional ultrasonic radar localization scanning system. Through programmatic control, the microcontrol unit (MCU) manages the emission and reception of ultrasonic pulse signals, transmitting detection data to a PC for processing. This process enables the visualization and analysis of spatiotemporal information during scanning and provides real-time obstacle position data with an error margin of less than 5 mm. With its array of compelling features, the DS-TAS represents a significant advancement in the acoustic sensing community and could have a wide range of applications in human-machine interaction and voice recognition.

* Corresponding authors.
*E-mail addresses:* yxi6@cqu.edu.cn (Y. Xi), jun.chen@ucla.edu (J. Chen).

[1] These authors contributed equally.

https://doi.org/10.1016/j.nanoen.2024.109638
Received 29 February 2024; Received in revised form 5 April 2024; Accepted 17 April 2024
Available online 26 April 2024
2211-2855/

## 2. Results and discussion

### 2.1. Mechanism and operating parameters of the DS-TAS

Fig. 1a displays a schematic diagram of the DS-TAS structure, which consists of two stainless steel electrode plates. These plates are strategically placed small to allow sound waves to pass through, causing displacement changes in the triboelectric film. The chosen material for the triboelectric film is fluorinated ethylene propylene (FEP), selected for its superior chemical resistance, heat resistance, crack resistance, high negative charge retention, and excellent triboelectric properties. The metal plates, adhered to both sides of the FEP film, are separated by plastic spacers, creating a symmetrical capacitive structure. This design enables both sides of the film to hold triboelectric charges, potentially doubling the overall triboelectric charge and, consequently, enhancing output. Physical images of the triboelectric film and the electrodes are shown in Fig. 1(b-c). Fig. 1d illustrates the electron cloud model for generating triboelectric charges [43,44]. Initially, when negatively triboelectric material E and positively triboelectric T are not in atomic-level contact, their electron clouds remain separate (Fig. 1d, first segment). Electrons are bound to orbit by potential wells, preventing transfer. Upon contact, electron clouds overlap, forming ionic or covalent bonds and shortening the bond length. This transforms the potential well into an asymmetric double potential well, reducing the potential barrier (Fig. 1d, second segment). Consequently, electrons transfer between atoms, generating triboelectric charges (Fig. 1d, third segment).

Acoustic waves are mechanical waves generated by vibrating sound sources. The “acoustic field” refers to the space through which these waves propagate. Fig. 1e simplifies a typical sound field, and Fig. 1f illustrates the relationship between the pressure at a point and its temporal changes, showing periodic variations in sound pressure, classified into three states (i-iii). Based on the principle of force interaction, we derive the DS-TAS working principles under periodic acoustic excitation, shown in Fig. 1g. This includes four states: (i) Negative maximum sound pressure (Figure 1ei) causes maximum film displacement to the left, with the left electrode accumulating maximum charge. (ii) Transition from the negative maximum (Figure 1ei) to equilibrium (Figure 1eii) results in an electrostatic equilibrium between electrodes. (iii) Positive maximum sound pressure (Figure 1eiii) causes maximum film displacement to the right, with the right electrode accumulating maximum charge. In most cases, the film oscillates between states i-iii. The current flow direction is depicted in fig. S1. The interaction between the electrode plates and the external circuit generates electrical voltage signals correlating with acoustic wave characteristics, completing a DS-TAS operation cycle. (iv) In extreme scenarios, like high sound pressure or strong airflows (fig. S2), the film contacts the metal electrode, generating triboelectric charges. Additionally, the DS-TAS is designed to be detachable, allowing for easy charging of the triboelectric film through manual contact electrification.

Regarding acoustic wave classification, Fig. 1h demonstrates that they are primarily categorized by frequency: infrasound (<20 Hz), audible (20 Hz to 20 kHz), and ultrasound (>20 kHz), each with varied applications. Therefore, triboelectric acoustic sensors responsive across an ultrawide frequency range hold significant potential for various applications. Fig. 1i compares this work with other triboelectric acoustic device research. We have achieved a continuous frequency response from 20 Hz to 58 kHz in ambient air and a sensitivity of 6.67 V/Pa, marking a significant milestone in triboelectric acoustic device research.

### 2.2. The output characteristics of DS-TAS within the audible acoustic wave

In the initial stage, we conducted a further theoretical analysis of the displacement distribution of the triboelectric film [21,40,45]. This was simplified as constrained motion within a two-dimensional circular plane with fixed boundaries. Consequently, we derived the equation for the forced motion of the circular film under the influence of acoustic waves as:

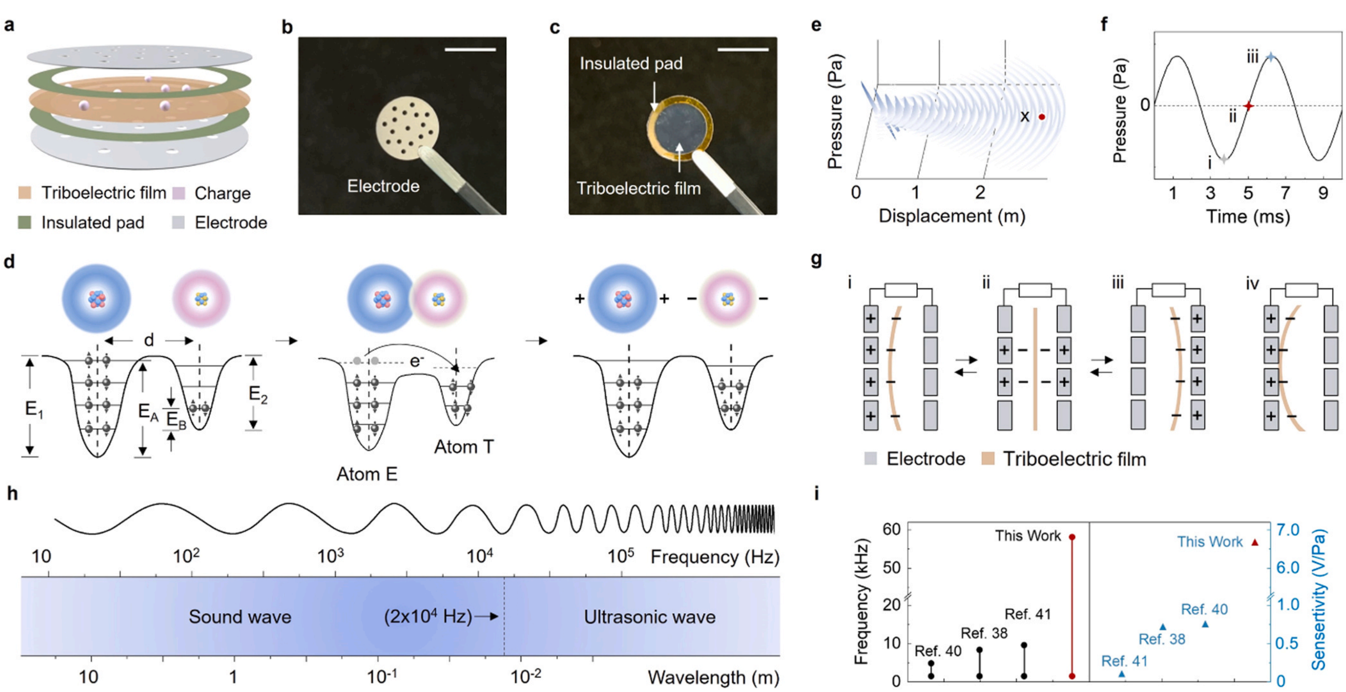


**Fig. 1. Device Structure and Working Principles.** (a) Presents a schematic representation of the device’s structure, detailing its components. (b, c) Feature photographs of the device with a scale of 1 cm. (d) Illustrates the fundamental principles of triboelectric charge generation using the overlapped electronic cloud model. (e) Shows a schematic representation of the distribution during simulated sound field propagation. (f, g) Display simulated images depicting pressure variations at fixed points within the sound field and the vibration modes of the membrane. (h) Provides continuous distribution diagrams of sound waves at different frequencies, highlighting the device’s response range. (i) Compares this work’s continuous frequency detection range and sensitivity against previous research, offering a comparative perspective.

$$Z(r,t) = \frac{p_0}{k^2 T}\left[\frac{J_0(kr)}{J_0(ka)} - 1\right]\exp(i\omega t) \quad (1)$$

where $J_0$ represents the Bessel function, $T$ is the film's tension per unit length, $k$ is the wave vector, $\omega$ is the angular frequency of the sound wave, $a$ is the max radius, $p_0$ is the sound pressure, $t$ is time and $r$ is the radius (for detailed derivation, please refer to Supplementary Note S1). Theoretical simulations were conducted with parameters including a radius of 5 mm, a tension of 3150 N/m, a surface density of 0.249 kg/m$^2$, an applied sound pressure of 1 Pa, and sound wave propagation perpendicular to the triboelectric film. To illustrate the vibrational patterns of the film at different frequencies, Fig. 2a depicts the displacement distribution under a 1 kHz sound wave. The maximum displacement at the central point is 6.4 nm, and the average displacement is calculated to be 3.77 nm. Two-dimensional cross-sectional images and displacement distribution projections are in fig. S3. The system is approximated as a parallel plate capacitor, and the voltage formula is given by:

$$U = E\overline{Z} \quad (2)$$

where $E$ is the electric field strength and $\overline{Z}$ is the average displacement (Supplementary Note S1). The output voltage, calculated using the Eq. (2), is 2.13 mV. However, the direct output of triboelectric signals is often challenging due to their diminutive scale, typically in the millivolt range. To overcome this and enable precise detection, a coupled amplification circuitry system is used. This system includes a transistor-based control section and an amplification unit (fig. S4), with photographs shown in fig. S5. The system's amplification performance for various frequencies is in fig. S6. Sinusoidal AC voltage signals with 20 mV amplitudes and 20 Hz to 200 kHz frequencies were applied through a function signal generator (fig S6a), with the amplification output shown in fig. S6b. The system displays stable performance for 0.2 kHz to 80 kHz frequencies, with adjustable gain. A Faraday electromagnetic cage, made of a metal enclosure, shields DS-TAS from external electromagnetic interferences (fig. S7a), according to its schematic diagram (fig. S7b), it is directly connected to the circular circuit

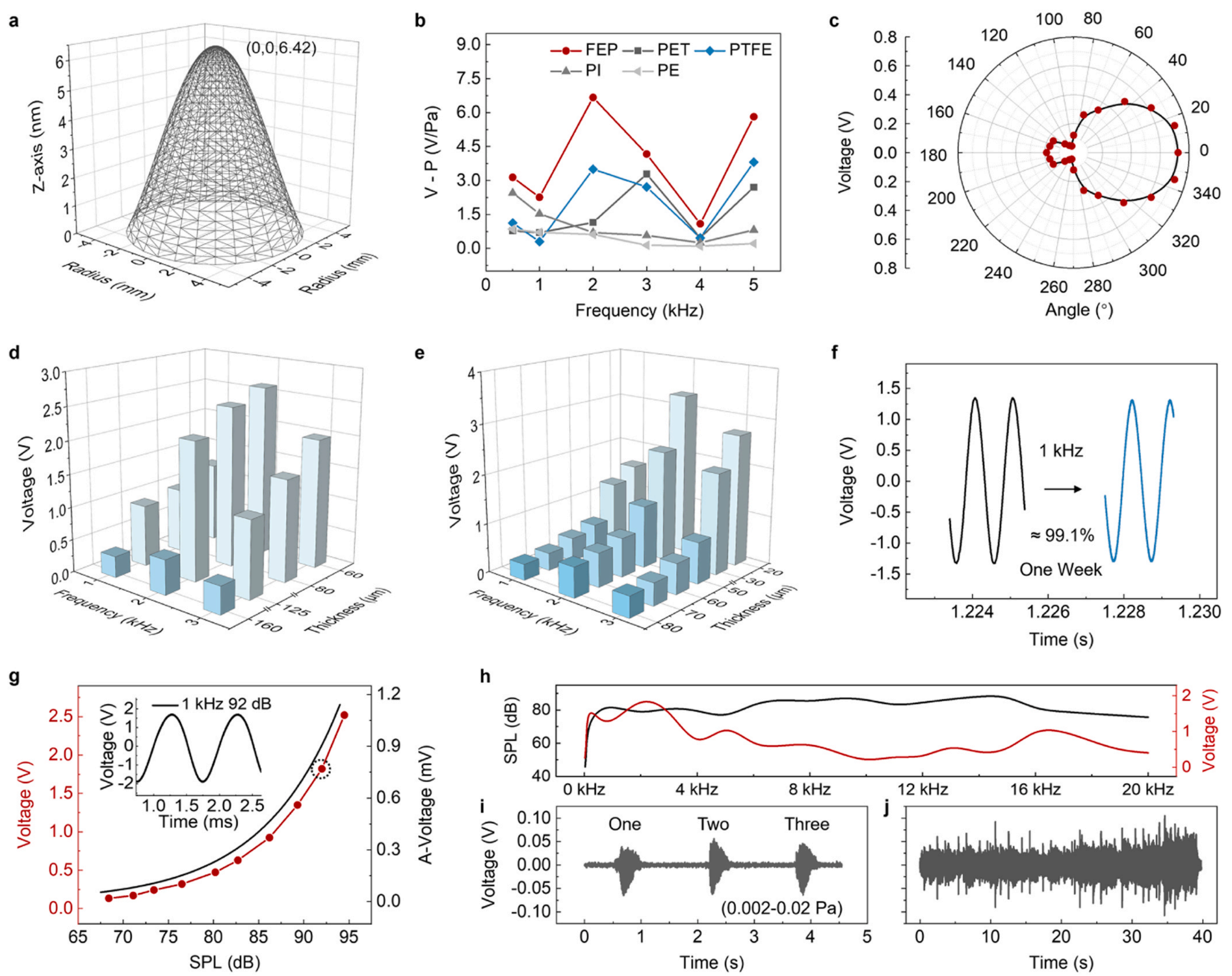


**Fig. 2. Performance Testing of the DS-TAS in the Audible Sound Frequency Range.** (a) Simulated illustration of forced vibration of the membrane at 1 kHz, showing the device's response to typical audible frequencies. (b) Output of different materials for friction films at various frequencies. (c) Response of DS-TAS to sound wave signals at different angles, showcasing its directional sensitivity. (d) Depicts DS-TAS performance with different thicknesses of insulating spacers, illustrating the impact of structural variations. (e) Performance of DS-TAS with triboelectric materials (FEP) of different thicknesses. (f) Presents stability testing results, indicating the device's reliability over time. (g) Relationship between output voltage and sound pressure level at a sound wave frequency of 1 kHz. (h) Displays the performance of DS-TAS across the audible sound frequency range from 20 Hz to 20 kHz. (i, j) Record human voices and music under low sound pressure (0.002–0.02 Pa corresponds to 40–60 dB), demonstrating the device's practical application in capturing audio.

board of the transistor section (fig. S5a, b). An external fixed structure (fig. S8) adds a detachable feature, enabling manual friction charging of the triboelectric film.

Fig. 2b presents the output performance for different triboelectric materials, with the measurement scenario in fig. S9. The test frequencies include 0.5, 1, 2, 3, 4, and 5 kHz. The triboelectric film has a 30 μm thickness and a 10 mm effective diameter. The relationship between sound pressure level (SPL) and sound pressure is expressed as:

$$SPL = 20\log\frac{p_e}{p_r}(dB) \tag{3}$$

where $p_e$ is the sound pressure and $p_r$ is the reference sound pressure ($2\times 10^{-5}$ Pa). FEP material outperformed others at all frequencies, achieving 6.67 V/Pa under a 2 kHz acoustic wave, thus being chosen for the DS-TAS triboelectric layer. Other triboelectric materials also exhibited different frequency response performances at the same frequency. Therefore, the variation in output performance is attributed to the inherent properties of the materials. The original voltage outputs for five materials are in fig. S10. Fig. 2c shows the output performance at different angles. DS-TAS was placed stationary at the center, with the sound source positioned at a 50 cm radius, measuring every 15° (fig. S11). The output is maximized at 0° and minimized at 90° (or 270°), indicating DS-TAS's directional characteristic. Fig. 2d explores output performance variation with different insulating spacer thicknesses (fig. S12), with the triboelectric membrane at 30 μm. Spacers made of PI material with thicknesses of 60, 80, 125, and 160 μm were tested at 1, 2, and 3 kHz frequencies. A 60 μm spacer yielded the best performance, while a 160 μm spacer had the lowest. Thus, a 60 μm spacer thickness was standardized. Fig. 2e examines output performance with different FEP thicknesses (fig. S13), testing 20, 30, 50, 60, 70, and 80 μm thicknesses with acoustic wave frequencies at 1, 2, and 3 kHz. The 20 μm thickness had the best output, with performance decreasing with increased thickness. For practicality, a 30 μm FEP membrane was chosen as the standard.

Fig. 2f highlights DS-TAS's stability. A 1 kHz acoustic wave with a stable SPL was applied, and the signal was measured one week apart. The latter signal retained 99.1 % of the initial signal's strength. Fig. 2g illustrates the output characteristics at different SPLs with a 1 kHz frequency. The output voltage increases exponentially with SPL, enabling low SPL detection. Raw voltage signals are in fig. S14, with the 92 dB waveform inset. The relationship between unamplified analog voltage and SPL follows Eqs. (1) and (2), showing a similar exponential trend in theory and experiment. Fig. 2h presents DS-TAS's responsiveness across 20 Hz to 20 kHz frequencies. A DS-TAS measurement video for a 4 kHz acoustic wave is in Supplementary Movie S1. DS-TAS maintains a continuous response to audible sound waves at every frequency, despite responsiveness fluctuations. Raw voltage waveforms at various frequencies are in fig. S15 to S17. Based on its response to sound pressure, Fig. 2i shows human voice recordings using DS-TAS under low sound pressure (0.002–0.02 Pa, 40–60 dB), including content labeled one, two, and three. Additionally, the famous music 'Going Home' was recorded under similar conditions (Fig. 2j), demonstrating DS-TAS's capability to effectively record both speech and music at low pressures. Spectral data for both are in fig. S18 and Supplementary Movie S2.

Supplementary material related to this article can be found online at doi:10.1016/j.nanoen.2024.109638.

### 2.3. The responsiveness of ultrasonic signals

To expand the detection capabilities of the DS-TAS for acoustic waves, particularly in the ultrasonic frequency range, we simulated the triboelectric film's displacement under ultrasonic waves at 40 kHz and 1 Pa pressure using Eq. (1). Fig. 3a shows this simulation. The two-dimensional cross-sectional curve and displacement distribution projection are provided in fig. S19. The maximum center point displacement decreased to 0.52 nm, indicating a change in vibrational mode at

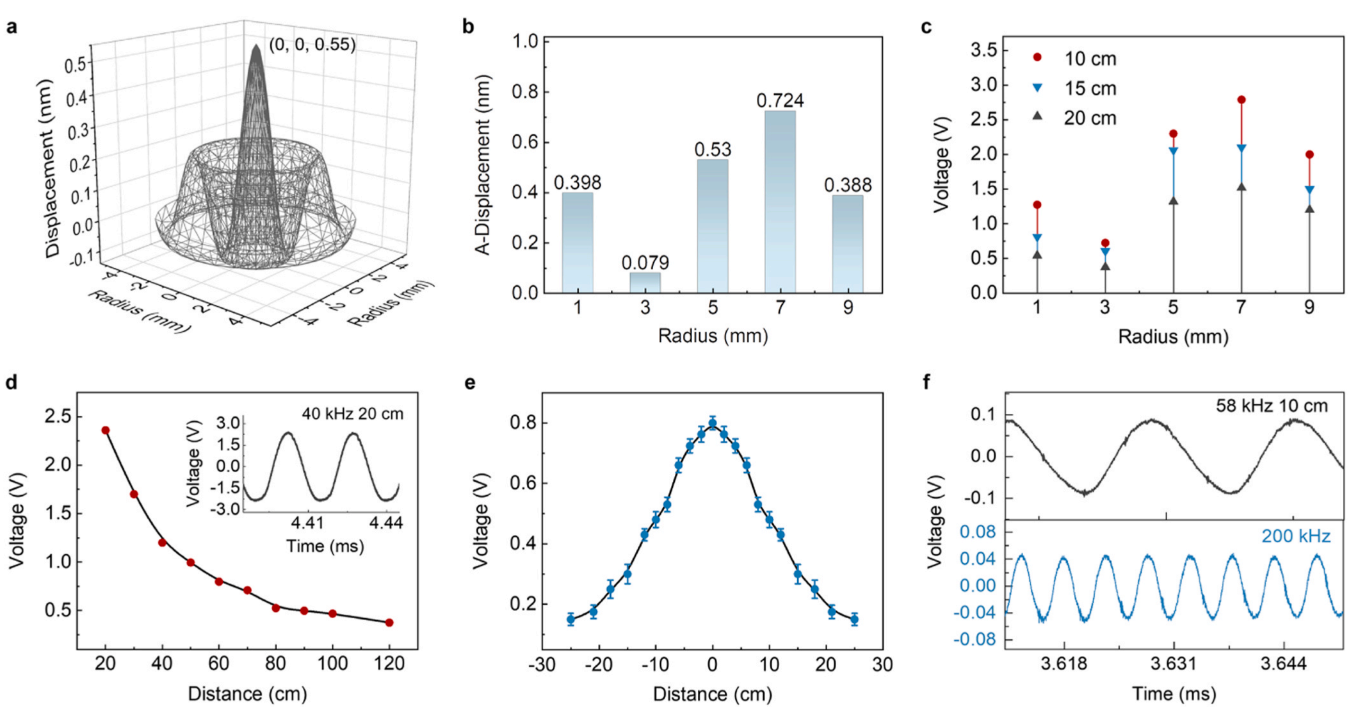


**Fig. 3. Response of DS-TAS to Ultrasonic Waves.** (a) Shows a simulated illustration of forced membrane vibration under ultrasonic waves at 40 kHz, highlighting the device's capability at higher frequencies. (b) Details theoretical average displacement magnitude of different effective radii, indicating the adaptability of DS-TAS to various ultrasonic conditions. (c) Visualizes ultrasonic voltage signals from DS-TAS with different radii at varying distances, showcasing the device's sensitivity and range. (d) Illustrates the relationship between output voltage and detection distance, offering insight into the device's effective range. (e) Displays output signal magnitude in the horizontal direction at a vertical distance of 50 cm from DS-TAS. (f) Captures ultrasonic detection signals at 58 kHz and 200 kHz, demonstrating the device's performance at high frequencies.

40 kHz, resulting in symmetric bending of the film. Relative to the simulated results at 1 kHz, the displacement magnitude has decreased significantly, indicating a decrease in output performance as the frequency increases. As per Eq. (1), the film's vibrational mode changes due to frequency and radius variations (fig. S20). Different ultrasonic frequencies have varied applications, so adjusting the device's radius can optimize film displacement for specific ultrasonic frequencies (fig. S21). Fig. 3b displays the simulated average displacement of the film with different effective radii under the same conditions as Fig. 3a. The radii tested were 1, 3, 5, 7, and 9 mm, with 7 mm yielding the maximum average displacement (0.724 nm). The simulated voltages for these radii are in fig. S22. The result shows that different effective radii of the film produce different displacement sizes under fixed frequency ultrasound. Therefore, the output can be improved by regulating the effective radius. For experimental verification, commercial ultrasonic transducers were used (fig. S23). We first examined the 25 kHz transducer (The rated SPL is 117 dB) by applying varying input frequencies at 23, 24, 25, 26, and 27 kHz. The strongest ultrasonic signal was observed at 25 kHz, confirming the transducer's single optimal transmission frequency (fig. S24). Fig. 3c shows the DS-TAS output voltage with different radii at 10, 15, and 20 cm distances, using a 40 kHz frequency transducer (The rated SPL is 117 dB). Measurement scenarios and videos are provided in fig. S25 and Supplementary Movie S3, respectively. The maximum output aligns with a 7 mm radius, consistent with theoretical predictions. However, for practicality, a 5 mm radius was chosen as the standard. Notably, at a distance of 120 cm, the output signal still had an amplitude of around 0.5 V, demonstrating DS-TAS's ability to detect ultrasonic signals in air at considerable distances (Fig. 3d). Fig. 3e illustrates ultrasonic detection in the horizontal direction at 50 cm from the transducer. The method is detailed in fig. S26. The central position had the highest output (~0.8 V), decreasing towards the sides. This suggests that 40 kHz ultrasonic signals propagate directionally, diverging conically. Finite element simulations of propagation range for different frequencies, showing directional characteristics, are in fig. S27. Higher frequencies exhibit stronger directionality. Fig. 3f presents waveforms of higher-frequency ultrasonic signals. The top part shows a 58 kHz (The rated SPL is 108 dB) signal at 10 cm with a 0.09 V amplitude, illustrating attenuation with higher frequencies in the air (fig. S28 and Supplementary Note S2). The bottom part depicts a 200 kHz (The rated SPL is 110 dB) signal detected through non-airborne transmission, with measurement scenarios in fig. S29.

Supplementary material related to this article can be found online at

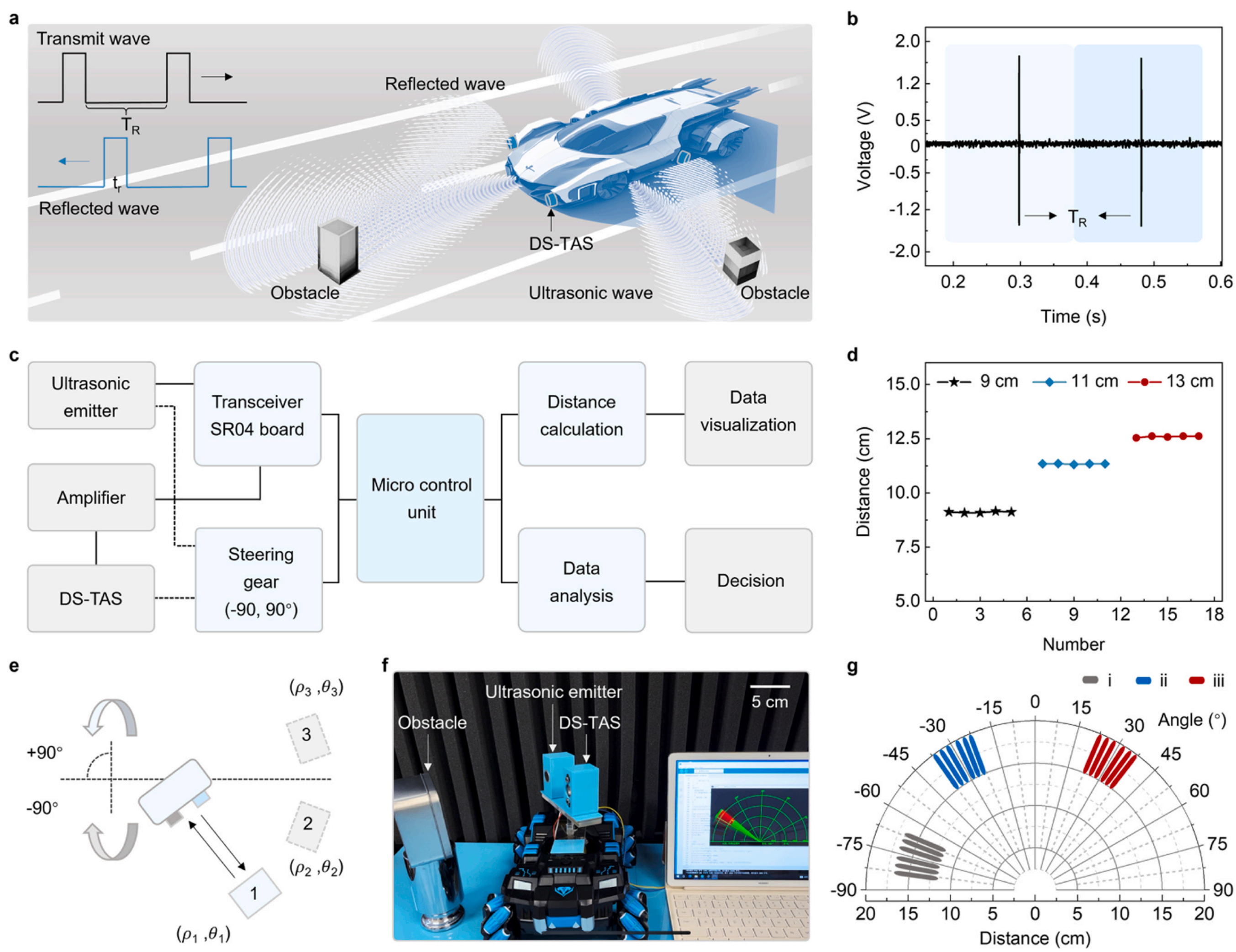


**Fig. 4. Application of the DS-TAS for a Real-time, Multi-directional Ultrasonic Radar System.** (a) Provides a conceptual representation of the ultrasonic radar system and pulse detection principle, illustrating its practical application. (b) Shows two adjacent typical pulse ultrasonic signals, allowing for an understanding of signal patterns. (c) Depicts a flowchart of the MCU-based ultrasonic radar detection system, outlining the operational process. (d) Measures obstacles at different distances using the DS-TAS-based ranging system in a fixed direction, demonstrating its accuracy. (e) Schematic illustrating the scanning range of the ultrasonic radar system and the distribution of obstacles. (f) Photograph of the ultrasonic radar system operating in real-time, providing a tangible sense of the setup. (g) Scanning results of obstacle positions, showcasing the system's effectiveness in real-world applications.

doi:10.1016/j.nanoen.2024.109638.

### 2.4. Application of DS-TAS in ultrasonic radar systems

Given DS-TAS's effective detection of directional ultrasonic signals, we developed an ultrasonic radar system based on it. Fig. 4a illustrates the system and signal propagation principles. Pulse ultrasonic waves are emitted by a transducer with a pulse width of $t_r$ (fig. S30), and the period $T_R$ (Fig. 4b). When an obstacle is in the path, the waves reflect and are detected by DS-TAS. The distance calculation principle is shown in fig. S31:

$$H = \frac{1}{2} v \Delta t \cos\left[\arctan\left(\frac{M}{H}\right)\right] \tag{4}$$

where $M$ is half the distance between the transducer and DS-TAS, $v$ is the speed of sound, and $\Delta t$ is the time between emission and reception. The distance between DS-TAS and the ultrasonic transducer is 10 cm (fig. S32, with detailed derivation in Supplementary Note S3). Fig. 4c presents the control flow of the multi-directional ultrasonic radar scanning system, integrating the sensor, data acquisition, transmission modules, MCU, and display module. The MCU controls the SR04 circuit board and a servo motor (fig. S33) to emit ultrasonic pulses and receive reflections detected by DS-TAS. The SR04 circuit comprises a transmitter port and a receiver port, where the transmitter port is connected to the ultrasonic generator, and the receiver port is connected to the output signal of DS-TAS. The servo motor drives the ultrasonic generator and DS-TAS to rotate and scan the area. When emitting an ultrasonic pulse signal, only the reflected ultrasonic signals within the period TR are detected, and the distance to obstacles is calculated accordingly. The servo motor enables spatial and temporal scanning within a (-90°, 90°) range. The MCU then transmits data to a PC for processing and visualization.

For system validation, measurements were conducted without the servo motor. Obstacles were placed at 9, 11, and 13 cm in the same direction, with errors in results being less than 5 mm, indicating high system accuracy (Fig. 4d). Fig. 4e shows a multi-directional measurement approach, with obstacles at (12 cm, −75°), (15 cm, −30°), and (15 cm, 30°). The detection module, controlled by the servo motor, performed spatial scanning. Real-time scanning images are in Fig. 4f, with an operational video in Supplementary Movie S4. Fig. 4g displays detection data for the three obstacle positions, confirming an error of less than 5 mm, showcasing the potential of the DS-TAS-based radar ranging system.

Supplementary material related to this article can be found online at doi:10.1016/j.nanoen.2024.109638.

## 3. Conclusions

We have proposed a symmetric double-sided capacitive triboelectric acoustic sensor (DS-TAS) strategy, demonstrating significant potential for applications in high-fidelity sound recording, human-machine interaction, and ultrasonic radar positioning. DS-TAS stands out due to its innovative design and fabrication, enabling a continuous response to audible sound waves ranging from 20 Hz to 20 kHz and detecting multiple ultrasonic frequencies (25, 40, 58, 200 kHz). By adjusting the effective radius, DS-TAS enhances its responsiveness to specific ultrasonic frequencies. Additionally, a coupled amplification circuitry system endows DS-TAS with high sensitivity to acoustic waves, reaching a remarkable 6.67 V/Pa, the highest value in the field of triboelectric acoustic sensors. DS-TAS has also proven its stability, maintaining 99.1 % of its output performance after one week of intermittent operation. Its detachable design facilitates easy manual friction charging, which extends its lifespan and reduces operational costs.

Exploiting DS-TAS's superior performance, we have successfully implemented it in a real-time, multi-directional ultrasonic radar positioning and scanning system. This system, controlled by programmed instructions, manages the emission and reception of ultrasonic pulse signals. The detection data is then transmitted to a PC for visualization, enabling spatial and temporal scanning. The radar system not only provides real-time obstacle position detection but also maintains an impressive accuracy, with an error margin of less than 5 mm.

Looking ahead, advancing triboelectric acoustic sensors could revolutionize fields like AI assistant interaction systems and big data collection. There is a growing need for further research to enhance sensor flexibility, miniaturization, and versatility to fit a broader range of application systems. The potential of triboelectric sensing-based acoustic technology is extensive, with promising implications in areas such as medical rehabilitation, intelligent industry, and environmental science. This highlights the importance of ongoing research and development in this rapidly evolving field.

## 4. Materials and methods

### 4.1. Manufacturing of the DS-TAS and radar system

DS-TAS is composed of two metal sensing electrodes (12 mm diameter, 1 mm thickness), a central triboelectric layer (12 mm diameter, 30 μm thickness), and two insulating pads (10 mm inner diameter, 12 mm outer diameter, 60 μm thickness). The triboelectric layers utilize various films including FEP, polytetrafluoroethylene (PTFE), polyethylene (PE), polyethylene terephthalate (PET), and polyimide (PI). The sensor's standard diameter is 12 mm unless specified otherwise. The Faraday electromagnetic cage, housing the sensor, is constructed with an aluminum shell and side openings. The amplification circuit board, model SFT-MC08, is equipped with an NE5532P chip. Signal acquisition is performed using a DS-Cope oscilloscope, boasting a 100 MHz bandwidth and a sampling rate of up to 1 Giga-sample per second.

The ultrasonic radar system incorporates an Arduino Uno R3 with an Atmel Atmega328P chip, controlling the servo motor and SR04 module. The servo motor, MG995, can rotate 180°. The SR04 module manages the emission and reception of ultrasonic pulse signals, and the ultrasonic transducer used is the TCT40–14BT. The visualization program is developed using Processing.

### 4.2. Characterization and measurement

The sensor's output was measured and recorded using an electrometer (Keithley 6514; TRKE 344-K) and an oscilloscope (DS-Cope, U2P20). Data collection involved speakers (R1700BT and PW5120) and various ultrasonic transducers (TCT25–16BT, 117 dB; TCT40–16BT, 117 dB; EU10POF58H07A, 108 dB; EU10PIF200H07T/R, 110 dB). A function signal generator (UTG962E) was also used. Videos were captured with an iPhone 13, and data processing was done on a MateBook-e workstation. FEP (F46, J. F. X. C. Technology Co., Ltd, China), PI (UO, S. H. T. X. Technology Co., Ltd, China), PE (M. C. Technology Co., Ltd, China), PET (M. C. Technology Co., Ltd, China), PTFE (S. H. P. Plastic Co., Ltd, China).

## CRediT authorship contribution statement

**Dahu Ren:** Writing – review & editing. **Farid Manshaii:** Writing – review & editing. **Xiao Xiao:** Investigation. **Huake Yang:** Investigation. **Jun Chen:** Supervision. **Yi Xi:** Supervision. **Shengyang Xiong:** Writing – review & editing. **Xuemei Zhang:** Writing – review & editing. **Qianying Li:** Writing – review & editing. **Junyi Yin:** Writing – review & editing. **Xiaochuan Li:** Writing – review & editing.

## Declaration of competing interest

The authors declare that they have no known competing financial interests or personal relationships that could have appeared to influence the work reported in this paper

## Data availability

Data will be made available on request.

## Acknowledgments

J.C. acknowledges the Henry Samueli School of Engineering & Applied Science and the Department of Bioengineering at the University of California, Los Angeles for the startup support. Y.X. acknowledges the NSFC (52272191, U21A20147, 52073037), the National Key R & D Project from Minister of Science and Technology (2021YFA1201602), and the Fundamental Research Funds for the Central Universities (Grant No. 2021CDJQY-005, 2022CCJJCLK001).

## Appendix A. Supporting information

Supplementary data associated with this article can be found in the online version at doi:10.1016/j.nanoen.2024.109638.

## References

[1] W.J. Zhou, et al., Sound induces analgesia through corticothalamic circuits, Science 377 (2022) 198–204.
[2] Z. Che, et al., Speaking without vocal folds using a machine-learning-assisted wearable sensing-actuation system, Nat. Commun. 15 (2024) 1873.
[3] N. Forrester, Sounds of science: how music at work can fine-tune your research, Nature 616 (2023) 399–401.
[4] A. Libanori, et al., Smart textiles for personalized healthcare, Nat. Electron. 5 (2022) 142–156.
[5] X. Fan, et al., Ultrathin, rollable, paper-based triboelectric nanogenerator for acoustic energy harvesting and self-powered sound recording, ACS Nano 9 (2015) 4236.
[6] J. Park, et al., Quadruple ultrasound, photoacoustic, optical coherence, and fluorescence fusion imaging with a transparent ultrasound transducer, Proc. Natl. Acad. Sci. U. S. A. 118 (2021) e1920879118.
[7] G. Chen, et al., Electronic textiles for wearable point-of-care systems, Chem. Rev. 122 (3) (2022) 3259–3291.
[8] G. Chen, et al., Smart textiles for electricity generation, Chem. Rev. 120 (8) (2020) 3668–3720.
[9] J. Yang, et al., Triboelectrification-based organic film nanogenerator for acoustic energy harvesting and self-powered active acoustic sensing, ACS Nano 8 (2014) 2649.
[10] J. Yin, et al., Smart textiles for self-powered biomonitoring, Med-X 1 (2023) 3.
[11] X. Xiao, et al., Bioinspired acoustic textiles with nanoscale vibrations for wearable biomonitoring, Matter 5 (2022) 1342–1345.
[12] Z. Lin, et al., A personalized acoustic interface for wearable human-machine interaction, Adv. Funct. Mater. 31 (2021) 2109430.
[13] J. Xu, et al., Acoustic metamaterials-driven transdermal drug delivery for rapid and on-demand management of acute disease, Nat. Commun. 14 (2023) 869.
[14] W. Deng, et al., Piezoelectric nanogenerators for personalized healthcare, Chem. Soc. Rev. 51 (2022) 3380–3435.
[15] K.J. Ma, et al., A wave-confining metasphere beamforming acoustic sensor for superior human-machine voice interaction, Sci. Adv. 8 (2022) eadc9230.
[16] Z.L. Wang, J. Chen, L. Lin, Progress in triboelectric nanogenerators as a new energy technology and self-powered sensors, Energy Environ. Sci. 8 (2015) 2250.
[17] J. Chen, Z.L. Wang, Reviving vibration energy harvesting and self-powered sensing by a triboelectric nanogenerator, Joule 1 (2017) 480.
[18] N. Zhang, et al., Progress in triboelectric nanogenerators as self-powered smart sensors, J. Mater. Res. 32 (2017) 1628.
[19] X. Zhao, H. Askari, J. Chen, Nanogenerators for smart cities in the era of 5G and Internet of Things, Joule 5 (2021) 1391–1431.
[20] Y. Fang, et al., Ambulatory cardiovascular monitoring via a machine-learning-assisted textile triboelectric sensor, Adv. Mater. 33 (2021) 2104178.
[21] R. Hinchet, et al., Transcutaneous ultrasound energy harvesting using capacitive triboelectric technology, Science 365 (2019) 491–494.
[22] S. Zhang, et al., Leveraging triboelectric nanogenerators for bioengineering, Matter 4 (2021) 845–887.
[23] K. Meng, et al., A wireless textile based sensor system for self-powered personalized health care, Matter 2 (2020) 896–907.
[24] Z. Zhou, et al., Sign-to-speech translation using machine-learning-assisted stretchable sensor arrays, Nat. Electron. 3 (2020) 571–578.
[25] Y. Zhou, et al., Self-powered sensing technologies for human metaverse interfacing, Joule 6 (2022) 1381–1389.
[26] J. Yin, et al., Self-powered eye-computer interaction via a triboelectric nanogenerator, Device 2 (2024) 00252.
[27] Y. Fang, et al., A deep-learning-assisted on-mask sensor network for adaptive respiratory monitoring, Adv. Mater. 34 (2022) 2200252.
[28] G. Conta, et al., Triboelectric nanogenerators for therapeutic electrical stimulation, Adv. Mater. 33 (2021) 2007502.
[29] Y. Su, et al., Self-powered respiration monitoring enabled by a triboelectric nanogenerator, Adv. Mater. 33 (2021) 2101262.
[30] R. Guo, et al., Deep learning assisted body area triboelectric hydrogel sensor network for infant care, Adv. Funct. Mater. 32 (2022) 2204803.
[31] S. Parandeh, et al., Advances in triboelectric nanogenerators for self-powered regenerative medicine, Adv. Funct. Mater. 31 (2021) 2105169.
[32] Z. Zhou, et al., Smart insole for robust wearable biomechanical energy harvesting in harsh environments, ACS Nano 14 (2020) 14126–14133.
[33] F. Sheng, et al., Wearable energy harvesting-storage hybrid textiles as on-body self-charging power systems, Nano Res. Energy 2 (2023) e9120079.
[34] X. Xiao, et al., Wearable triboelectric nanogenerators for therapeutics, Trends Chem. 3 (2021) 279–290.
[35] X. Pu, C. Zhang, Z.L. Wang, Triboelectric nanogenerators as wearable power sources and self-powered sensors, Natl. Sci. Rev. 10 (2023) nwac170.
[36] J.Q. Zheng, et al., Acoustic core-shell resonance harvester for application of artificial cochlea based on the piezo-triboelectric effect, ACS Nano 15 (2021) 17499–17507.
[37] S. Pyo, J. Lee, K. Bae, S. Sim, J. Kim, Recent progress in flexible tactile sensors for human-interactive systems: from sensors to advanced applications, Adv. Mater. 33 (2021) 2005902.
[38] J. Park, et al., Frequency-selective acoustic and haptic smart skin for dual-mode dynamic/static human-machine interface, Sci. Adv. 8 (2022) eabj9220.
[39] H.F. Zhao, et al., Underwater wireless communication via TENG-generated Maxwell's displacement current, Nat. Commun. 13 (2022) 3325.
[40] H.Y. Guo, et al., A highly sensitive, self-powered triboelectric auditory sensor for social robotics and hearing aids, Sci. Robot. 3 (2018) eaat2516.
[41] S. Kang, et al., Transparent and conductive nanomembranes with orthogonal silver nanowire arrays for skin-attachable loudspeakers and microphones, Sci. Adv. 4 (2018) eaas877.
[42] C. Chen, et al., Micro triboelectric ultrasonic device for acoustic energy transfer and signal communication, Nat. Commun. 11 (2020) 4143.
[43] C. Xu, et al., On the electron-transfer mechanism in the contact-electrification effect, Adv. Mater. 30 (2018) 1706790.
[44] X.C. Qu, et al., Artificial tactile perception smart finger for material identification based on triboelectric sensing, Sci. Adv. 8 (2022) eabq2521.
[45] Z. Zhang, J. Shao, Y. Nan, M. Willatzen, Z.L. Wang, Theory and shape optimization of acoustic driven triboelectric nanogenerators, Mater. Today Phys. 27 (2022) 100784.